RAA 2014 Vol. **14** No. **4**, 411–422 doi: 10.1088/1674–4527/14/4/004
http://www.raa-journal.org *http://www.iop.org/journals/raa*

Research in Astronomy and Astrophysics

Prompt optical emission from gamma-ray bursts with multiple timescale variability of central engine activities *

Si-Yao Xu[1] and Zhuo Li[1,2]

[1] Department of Astronomy and Kavli Institute for Astronomy and Astrophysics, Peking University, Beijing 100871, China; *syxu@pku.edu.cn*
[2] Key Laboratory for the Structure and Evolution of Celestial Objects, Chinese Academy of Sciences, Kunming 650011, China

Received 2013 September 9; accepted 2013 November 8

Abstract Complete high-resolution light curves of GRB 080319B observed by *Swift* present an opportunity for detailed temporal analysis of prompt optical emission. With a two-component distribution of initial Lorentz factors, we simulate the dynamical process of shells being ejected from the central engine in the framework of the internal shock model. The emitted radiations are decomposed into different frequency ranges for a temporal correlation analysis between the light curves in different energy bands. The resulting prompt optical and gamma-ray emissions show similar temporal profiles, with both showing a superposition of a component with slow variability and a component with fast variability, except that the gamma-ray light curve is much more variable than its optical counterpart. The variability in the simulated light curves and the strong correlation with a time lag between the optical and gamma-ray emissions are in good agreement with observations of GRB 080319B. Our simulations suggest that the variations seen in the light curves stem from the temporal structure of the shells injected from the central engine of gamma-ray bursts. Future observations with high temporal resolution of prompt optical emission from GRBs, e.g., by UFFO-Pathfinder and SVOM-GWAC, will provide a useful tool for investigating the central engine activity.

Key words: gamma rays: bursts — GRB 080319B

1 INTRODUCTION

Gamma-ray bursts (GRBs) are believed to be produced by the relativistic jets released from compact central engines, however the composition of jets and the energy dissipation and radiation mechanism at work are still far from clear. In the widely used internal shock model (Rees & Meszaros 1994), the energy dissipation in GRBs is caused by collisions between different parts of the unsteady outflow. These collisions produce shocks which accelerate electrons and generate a magnetic field, and the GRB prompt emission is produced by synchrotron radiation from the accelerated electrons. The internal shock model can generally match the gamma-ray properties of GRBs. For typical model parameters, the internal shock synchrotron model can naturally explain the complexity of GRB light

* Supported by the National Natural Science Foundation of China.

curves (Kobayashi et al. 1997), the spectral break energy around the MeV range, and the high energy photon index of $\beta \sim -2$ (see the review by Waxman 2003)[1]. Moreover the "fast cooling problem" of the low energy photon index can also be reconciled by incorporating a postshock magnetic field decay in the internal shock model (Pe'er & Zhang 2006; Zhao et al. 2013).

The observations of GRB prompt emission outside the MeV energy range will further help to diagnose the jet properties and the central engine activity. Observations of bright GRBs by *Fermi*-LAT reveal that GRB emission in the GeV range also shows short timescale, $\lesssim 1$ s, variabilities in both long and short GRBs (e.g., Abdo et al. 2009a,b), implying there is a similar origin with the MeV emission. However, the temporal delay of GeV emission relative to the MeV one implies the GeV emission is radiated at larger radii than the MeV emission (Li 2010). Moreover, the fact that the GeV emission is dominated by the MeV emission supports that the radiation mechanism at work for MeV emission is synchrotron radiation other than inverse Compton scattering (Wang et al. 2009; see also Derishev et al. 2001; Piran et al. 2009). On the other hand, the prompt optical emission during the gamma-ray emission is detected in some GRBs (e.g., GRB 990123, Akerlof et al. 1999; GRB 041219A, Vestrand et al. 2005; GRB 051109A and GRB 051111, Yost et al. 2007; GRB 061121, Page et al. 2007; see also Kopač et al. 2013 and references therein). The bright optical emission also implies that the radius of the optical emission region is larger than that of the MeV emission region, in order to avoid synchrotron self absorption (Li & Waxman 2008; Fan et al. 2009; Shen & Zhang 2009; Zou et al. 2009). However the temporal optical properties on a short timescale, $\lesssim 1$ s, are not clear due to the low time resolution in optical observations.

By luck, the detection of the naked-eye burst GRB 080319B presents the only and best-sampled case hitherto for analyzing the overall temporal structure of light curves from GRBs (Racusin et al. 2008; Beskin et al. 2010). The data with high (sub-second) temporal resolution, acquired from the onset of the optical transient to the end, make it possible to use this burst to reveal detailed structure in the optical emission, shedding light on the behavior of the burst's internal engine (Beskin et al. 2010). There are two main temporal properties in the optical light curve of GRB 080319B. First, the onset of the optical emission is delayed relative to the gamma-ray case by ~ 10s; Second, in the plateau phase the optical light curve is correlated with the gamma-ray one but with a time lag of ~ 2 s. The former property may be due to the effect of the environment, e.g., the effect of dust in the molecular cloud (Cui et al. 2013), while the latter is more likely tracking the time history of the central engine, which is the focus of this paper.

As pointed out in Li & Waxman (2008), within the context of internal shock models, after the first generation collisions that produce gamma-ray emission occur, collisions continue to happen at progressively larger radii with progressively smaller relative velocities. These "residual collisions" produce emission with progressively longer wavelengths, which can avoid the strong synchrotron absorption in the gamma-ray emission region and produce strong optical emission as observed. Because of the larger radii, the optical emission is expected to be systemically delayed relative to the gamma-ray case. Moreover, the correlation between optical and gamma-ray light curves in GRB 080319B implies that there is a large timescale of modulation in the central engine activity.

In this paper, we carry out numerical simulations of internal shocks to produce multi-band light curves, including gamma-ray and optical cases, with a focus on the effect of multiple timescale activities of the central engines. In Section 2, we provide a general description of the model we use. In Section 3, based on the model, we perform several simulated tests with different distributions of the initial Lorentz factor (LF), following which we derive both optical and gamma-ray light curves with different temporal structures. In Section 4, we compare the model results with the observational data of GRB 080319B. We discuss implications on central engine activity in Section 5, and draw our conclusions in Section 6.

[1] Note, there are also other energy dissipation models incorporating dissipation of magnetic energy by processes like reconnection, turbulence, etc. (e.g., Usov 1994; Thompson 1994; Lyutikov & Blandford 2003; Narayan & Kumar 2009; Zhang & Yan 2011) and other radiation mechanisms, e.g., thermal radiation (Mészáros & Rees 2000; Beloborodov 2010).

2 MODEL

Unsteady outflow from a GRB can be approximated by a set of individual shells with initial position r_i, mass m_i, LF γ_i and width Δ_i ($i = 1, ..., N$) at time $t = 0$. The initial widths can be taken to be the size of the source, $\Delta_{1,...,N} = \Delta_0 \approx 10^6\,\mathrm{cm}$. Given the initial condition of the shells, the subsequent dynamical evolution will be totally determined. Two neighboring shells i and $i+1$ which satisfy $v_{i+1} > v_i$ may collide at a time $t + \Delta t$, where $\Delta t = (r_i - r_{i+1})/(v_{i+1} - v_i)$, and the radius where the collision occurs is $r_c = r_i + v_i\Delta t = r_{i+1} + v_{i+1}\Delta t$. The pair of shells with a smaller Δt will collide first and merge into a new shell.

For the pair of colliding shells, the velocity of the center of momentum (c.m.) is

$$\beta_{\rm cm} = \sum \gamma_i\beta_i m_i / \sum \gamma_i m_i = \sum m_i\sqrt{\gamma_i^2 - 1} / \sum \gamma_i m_i$$

and the relevant LF is

$$\gamma_{\rm cm} = 1/\sqrt{1 - \beta_{\rm cm}^2}\,.$$

They are also the velocity and LF of the merged shell, respectively. In the case of $\gamma_{i,i+1} \gg 1$, the LF of the c.m. can be approximated by

$$\gamma_{\rm cm} = \sqrt{\frac{\gamma_i m_i + \gamma_{i+1} m_{i+1}}{m_i/\gamma_i + m_{i+1}/\gamma_{i+1}}}\,. \tag{1}$$

The shell may expand and change its width. Before collision at r_c, the width of a shell is $\Delta_i = \max(\Delta_i,\ r_c/\gamma_{\rm cm}^2)$ (Guetta et al. 2001). Because of compression by the shocks, the width of the merged shell right after shock crossing, Δ_c, is smaller than the sum of the shell widths right before the collision $\Delta_c < \Delta_i + \Delta_{i+1}$. (We derive Δ_c in the appendix.) After merging, the parameters for the merged shell are the position r_c, mass $m_i + m_{i+1}$, LF $\gamma_{\rm cm}$ and width Δ_c. Collisions continue to occur, and they will only stop when the velocities of the shells are increasing with radius after enough collisions and momentum exchanges between shells.

The internal energy generated in this collision is

$$E_{\rm in}/c^2 = (\gamma_i m_i + \gamma_{i+1} m_{i+1}) - \gamma_{\rm cm}(m_i + m_{i+1})\,, \tag{2}$$

which is released by synchrotron radiation. The emission appears as a pulse in the light curve. For simplicity, we assume the shape of the pulse to be a rectangle with a width of $\delta t = r_c/2\gamma_{\rm cm}^2 c$. So, the luminosity of the pulse in the light curve is $L = E_{\rm in}/\delta t$. Actually, a pulse with a fast rise and slower decline in its light curve can be produced due to the effect of an equal arrival time surface (e.g., Kobayashi et al. 1997; Shen et al. 2005; Huang et al. 2007). However, the time resolution of the observed light curves in the prompt phase is not sufficient to tell the detailed shape of a pulse. Thus we adopt a simple shape for each pulse and this assumption does not affect our temporal analysis of the light curves. In the observation, the starting time of the pulse is at an observer time of

$$t_{\rm obs} = t - r_c/c\,. \tag{3}$$

For the numerous collisions taking place between multiple shells, we superimpose pulses produced by each collision according to their time sequence.

Let us calculate the characteristic energy of the synchrotron photons. The velocity and LF of shell i in the c.m. frame are

$$\beta' = \frac{\beta_i - \beta_{\rm cm}}{1 - \beta_i\beta_{\rm cm}}, \qquad \gamma' = \gamma_i\gamma_{\rm cm}(1 - \beta_i\beta_{\rm cm})\,. \tag{4}$$

The characteristic LF of a postshock electron is

$$\gamma_e \approx (\gamma' - 1)\epsilon_e m_p/m_e + 1\,, \tag{5}$$

where ϵ_e is the fraction of postshock energy carried by electrons. The magnetic field in the shock frame is given by

$$B = \sqrt{\frac{2\epsilon_B E_{\rm in}}{\gamma_{\rm cm}^2 r_c^2 \Delta_c}}\,, \tag{6}$$

where ϵ_B is the fraction of postshock energy carried by the magnetic field. Note here we use the shock-compressed width Δ_c (derived in the appendix) to calculate B. The synchrotron photon energy is then

$$\epsilon_{\rm syn} \approx \gamma_{\rm cm}\gamma_e^2 \frac{heB}{2\pi m_e c} = \gamma_e^2 \frac{he}{2\pi m_e c}\sqrt{\frac{2\epsilon_B E_{\rm in}}{r_c^2 \Delta_c}}\,, \tag{7}$$

which is independent of $\gamma_{\rm cm}$. The equipartition values $\epsilon_e = \epsilon_B = 1/3$ will be used in the following numerical simulation.

For emission of long wavelengths, the synchrotron absorption may be important. Following Li & Waxman (2008) to calculate the synchrotron absorption frequency when $\epsilon_a > \epsilon_{\rm syn}$, we have

$$\epsilon_a = 2(\epsilon_B E_{\rm in})^{1/14}\gamma_{\rm cm}^{4/7}\gamma'^{2/7}(m_i + m_{i+1})^{2/7}(cr_c)^{-5/7}\Delta_c^{-5/14}{\rm keV}\,, \tag{8}$$

where a flat electron distribution with $p = 2$ is used. The energy spectrum will peak at $\epsilon = \max(\epsilon_{\rm syn}, \epsilon_a)$. For simplicity let us represent the spectrum by a δ function, i.e., the radiation is emitted at ϵ.

In order to inspect the temporal correlation between the prompt optical and gamma-ray emissions, the radiation produced by the collisions is decomposed into different frequency ranges that include gamma-ray (> 100 keV), X-ray ($1 - 10$ keV) and optical emission ($1 - 10$ eV), according to the energy band at which the synchrotron emission peaks.

3 SIMULATED TESTS

In order to show the effect of multi-timescale variabilities on the dynamics of the outflow, we carry out simulations for both cases of single- and two-timescale variabilities for comparison. We consider a series of individual material shells $i = 1, 2, ..., N$, with total number of shells N, released during a duration of time $T = 20$ s, so that the interval between two nearby shells is $\tau_1 = T/N$. The shells have equal masses but different LFs. We carry out four simulated tests as described below. For Test 1, we use $N = 2000$, thus $\tau_1 = 10$ ms, and the bulk LF of each shell follows

$$\log\gamma_i = \log 50 + \xi_i \log 10 + (2\xi_i - 1)\log 2\,, \tag{9}$$

where ξ_i is a random number between zero and unity. This is the case with only a single timescale of $\tau_1 = 10$ ms. For Test 2, there are two timescales in the evolution of the LF. Besides the $\tau_1 = 10$ ms variability ($N = 2000$), there is an additional slow modulation of $\tau_2 = 5$ s,

$$\log\gamma_i = \log 50 + \xi_i \log 10 + \sin\left[\frac{2\pi}{\tau_2}(i-1)\tau_1 - 1.5\right]\log 2\,. \tag{10}$$

We also perform Tests 3 and 4 in a similar way to Test 2 but with different values of τ_1 or τ_2: $\tau_1 = 10$ ms and $\tau_2 = 3.3$ s in Test 3; while $\tau_1 = 40$ ms (i.e., $N = 500$) and $\tau_2 = 5$ s in Test 4.

3.1 Test 1

To examine the dependence of the temporal structure of light curves on initial variations in the velocity inside the ejecta, we first perform a simulated test using a succession of initial LFs with only one component that shows rapid random variability. We consider the case with uniformly distributed

Table 1 Parameters and Results of the Simulation Tests

	N[1]	τ_1 (s)[2]	τ_2 (s)[3]	r[4]	Δt (s)[5]	δt_0 (s)[6]	$\delta t_{0,1}$ (s)[7]	$\delta t_{0,2}$ (s)[8]	δt_γ (s)[9]
Test 1	2000	0.01	–	0.56	0.8	2.8	1.4	12.9	0.004
Test 2	2000	0.01	5	0.50	1.9	3.0	1.3	15.0	0.004
Test 3	2000	0.01	3.3	0.65	1.4	2.3	1.4	13.5	0.006
Test 4	500	0.04	5	0.21	2.7	6.0	1.9	22.0	0.012
Test 5	2000	0.01	5	0.64	1.2	2.8	1.7	11.7	0.005

[1] The number of shells. [2] The timescales of the components with fast variability in initial LFs. [3] The timescales of the components with slow variability in initial LFs. [4] The highest correlation coefficient between optical and gamma-ray light curves. [5] The time lag between optical and gamma-ray emission. [6] The average timescale of variability in optical emission. [7] The average timescale of variability in optical emission for $t_{\rm obs} \leq 20$ s. [8] The average timescale of variability in optical emission for $t_{\rm obs} > 20$ s. [9] The average timescale of variability in gamma-ray emission.

LFs presented in Figure 1. Note that here we only display the first 20 s of the optical light curve for a clear comparison with the gamma-ray case. It is straightforward to show that the short-scale variability features of the LFs are imprinted on both the optical and gamma-ray light curves (Fig. 1). In contrast to the broad periodic component seen in the following simulated tests, there are only stochastic spikes in the light curves.

In addition, Figure 2 shows the complete optical light curves from our five simulated tests. Logarithmic luminosity is used here due to the weak optical emission after $t_{\rm obs} > 20$ s. The optical emission clearly has a more variable temporal profile in the first 20 s than in the remaining part (also see Table 1), i.e., variability timescale in the late part of the emission is larger than in the early part (< 20 s) of the emission.

3.2 Test 2

We start with a simple two-component LF distribution for the shells. Figure 3 presents the distribution of the initial LFs of the shells with indices from one to N. In our calculations, the Nth shell is the first shell emitted by the inner engine, indicating the outer edge of the ejecta. The overall duration of the burst is $T = 20$ s in the observer frame. The slow and periodic variability existing in the LFs is on a timescale of $\tau_2 = 5$ s, and the overlapping rapid and irregular variations have a timescale of $\tau_1 = 10$ ms. Figure 3 shows the corresponding optical and gamma-ray light curves produced by a Monte Carlo simulation of the dynamic process of the colliding shells we described in Section 2.

By comparing these two light curves, we find that they both show a superposition of two variable components: a slow periodic component with a duration of ~ 5 s and a fast component with stochastic short pulse widths. But in contrast to the smoother profile in the optical band, the gamma-ray light curve is obviously highly variable with more rapid short-scale variabilities (see Table 1). To have a better comparison with the observed data, we rebinned the optical and gamma-ray light curves with a 0.13 s and 50 ms bin size, respectively (Beskin et al. 2010), and performed a cross-correlation analysis between them. Figure 3 displays the normalized cross-correlation sequence between the optical and gamma-ray light curves as a function of optical delay time. The correlation coefficient reaches its highest value (~ 0.50) when the optical flux is delayed by 1.9 s with respect to the gamma-ray emission. Since our results are just based on the simple modeling of the internal shock dynamics, the time delay naturally results from the evolution of fluctuations in the LF of the fast moving shells. At first, gamma-ray emission originates from the outflow with highly variable LFs at a small radius. As the flow moves forward to a larger radius, the variance of the LFs of the remaining shells decreases, leading to a decrease in the radiated energy after collisions, as well as a decrease in the characteristic frequency of emission (Li & Waxman 2008).

The average ratio of the optical and gamma-ray fluxes indicates relatively bright optical emission accompanying gamma-ray emission, which is consistent with optical detections. The bright optical

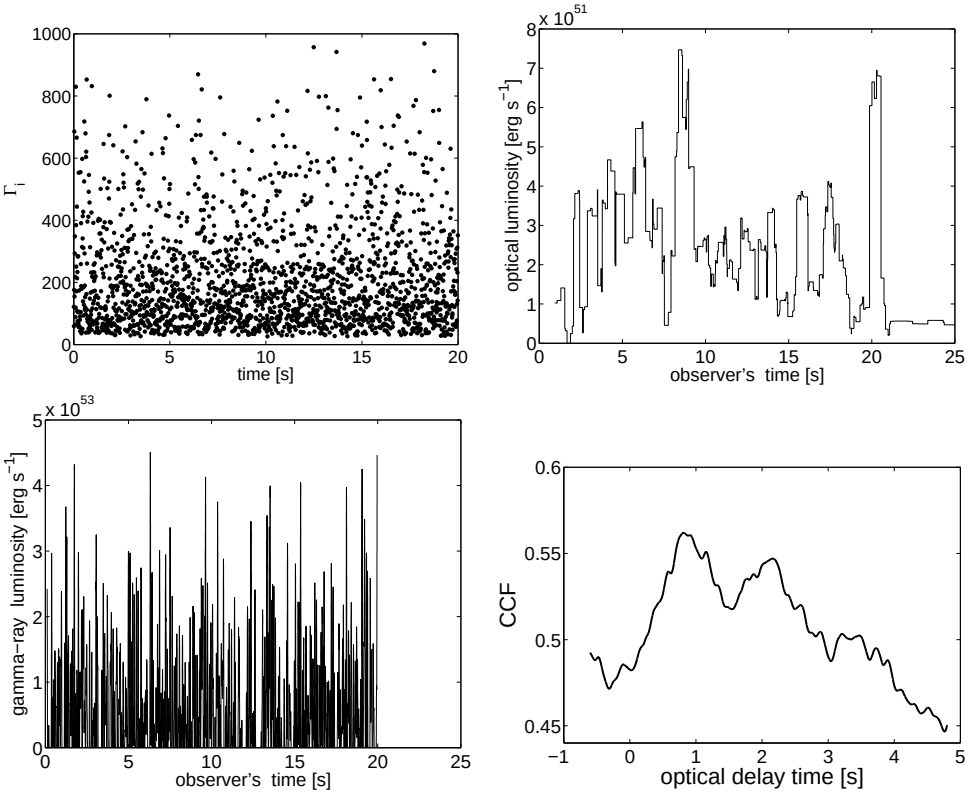

Fig. 1 Results of Test 1. *Top left*: the initial LF distribution. *Top right*: the optical light curve. *Bottom left*: the gamma-ray light curve in time bins of 50 ms. *Bottom right*: the cross-correlation function between the gamma-ray and optical light curves.

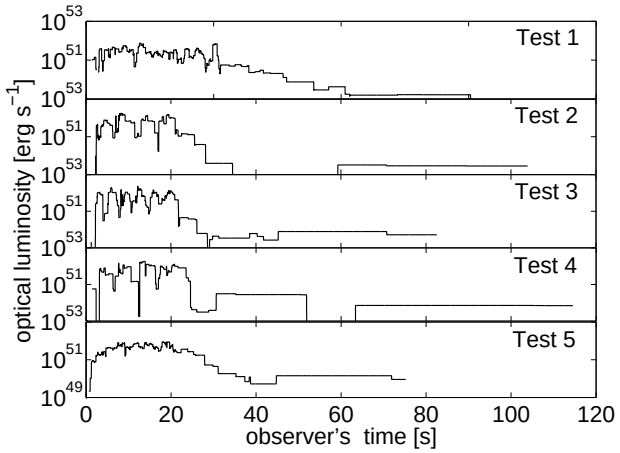

Fig. 2 The complete optical light curves from all simulation tests.

emission can be naturally explained in the framework of the model with residual collisions, since optical emission can be produced at large radii, where the optical depth for optical photons is low (Li & Waxman 2008).

3.3 Test 3

Next, we test the cases with different timescales of the two variability components of the initial LFs. This is the same as Test 2, except the period of the component with slow variability is changed to 3.3 s.

Figure 4 shows the resulting optical and gamma-ray light curves. Similar results to those presented in Figure 3 can be found for both light curves. With a shorter duration for the slow component (~ 3.3 s), the light curves contain the same number of periodic variabilities seen in the initial LFs.

3.4 Test 4

We then increase the timescale of the rapid variability in the initial LFs by reducing the number of shells. Correspondingly, the irregular short-scale variabilities in both light curves clearly have larger timescales. We find that the total energy emitted over the gamma-ray band obviously decreases due to fewer collisions at small radii (see Fig. 5). Fewer gamma-ray data also lead to a lower correlation between the two light curves.

Table 1 lists the parameters for the above simulation tests. Here we do not consider the redshift of the source, otherwise all timescales in Table 1 should be increased by $1 + z$. As can be seen from our simulation tests, the temporal behavior of prompt optical and gamma-ray emission is sensitive to the changes in variations of the initial velocity inside the ejecta. The variability features exhibited in light curves tend to strictly track the temporal structure of the initial LFs of the shells.

4 COMPARISON WITH GRB 080319B

The detection with high temporal resolution of the prompt optical emission from GRB 080319B and its gamma-ray counterpart serve as the only available observed data to test our model. Periodic variability on a timescale of a few seconds may exist in both optical and rebinned gamma-ray light curves during the prompt phase of the emission (Beskin et al. 2010). Besides the four similar peaks, variability on a short timescale can be seen in the realistic light curves, including the rapid optical variability on timescales from several seconds to subseconds and a large amount of stochastic variability in the gamma-ray emission (Beskin et al. 2010).

In agreement with observations, the simulated light curves capture both the underlying equidistant broad component and the features with short-scale variability. The detected time delay (~ 2 s in the observer frame, Beskin et al. 2010) between the optical and gamma-ray emission has the same order of magnitude as Δt shown in Table 1 (after being multiplied by $1 + z$). Despite the time lag, a clear similarity exists between the optical and gamma-ray light curves, as indicated in Beskin et al. (2010). This temporal correlation demonstrates that the emission in optical and gamma-ray ranges is generated by a common mechanism, but at different locations.

Since our model can be applied to general GRB events by modifying the initial LF distribution of the ejected shells, in order to construct the temporal structure of this specific burst, we also present a slightly modified version of Test 2 (see Test 5 in Table 1 and Fig. 6) as a comparison with figure 2 in Beskin et al. (2010). Note that the initial LFs in Test 5 have the same variability timescales as those in Test 2, but the adjusted LF distribution leads to different light curves, mainly characterized by four overlapping peaks (Fig. 6) instead of separated pulses (Fig. 3).

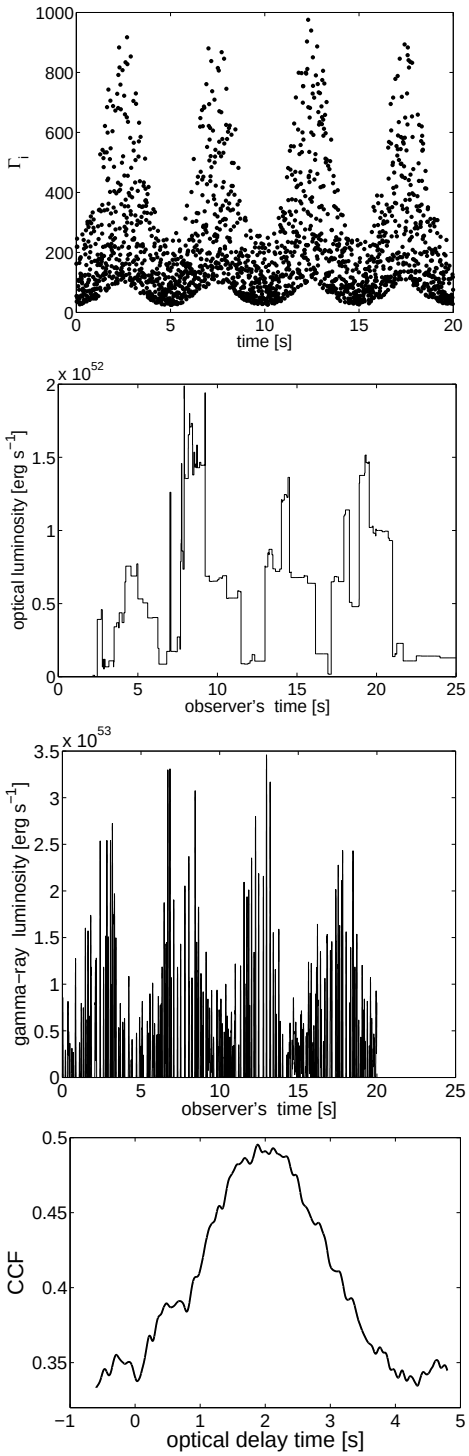

Fig. 3 Results of Test 2. The respective panels represent the same quantities as in Fig. 1.

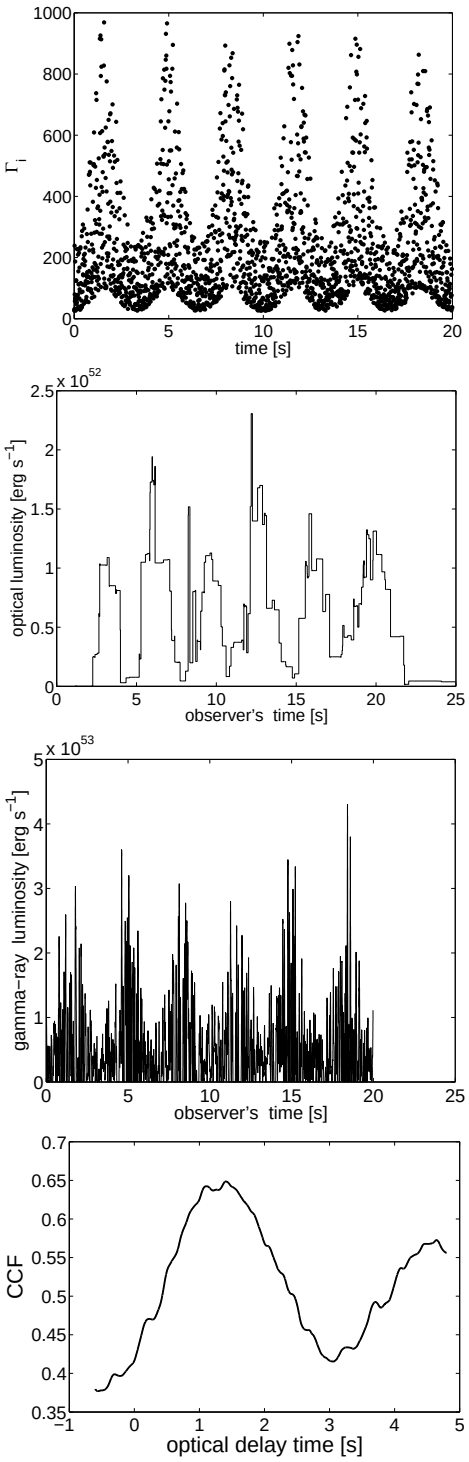

Fig. 4 Results of Test 3. The respective panels represent the same quantities as in Fig. 1.

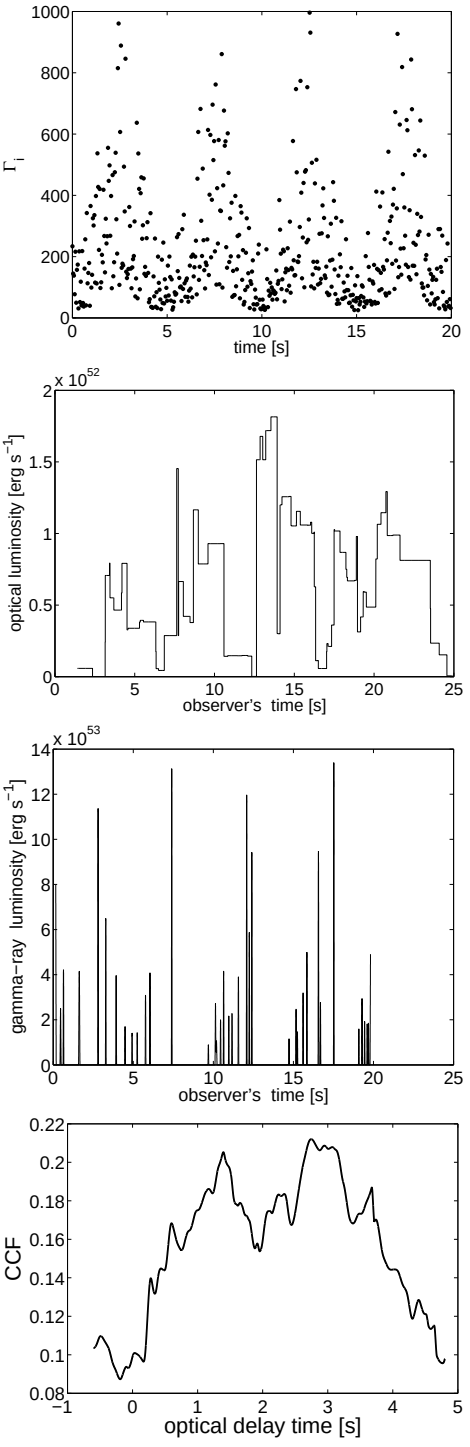

Fig. 5 Results of Test 4. The respective panels represent the same quantities as in Fig. 1.

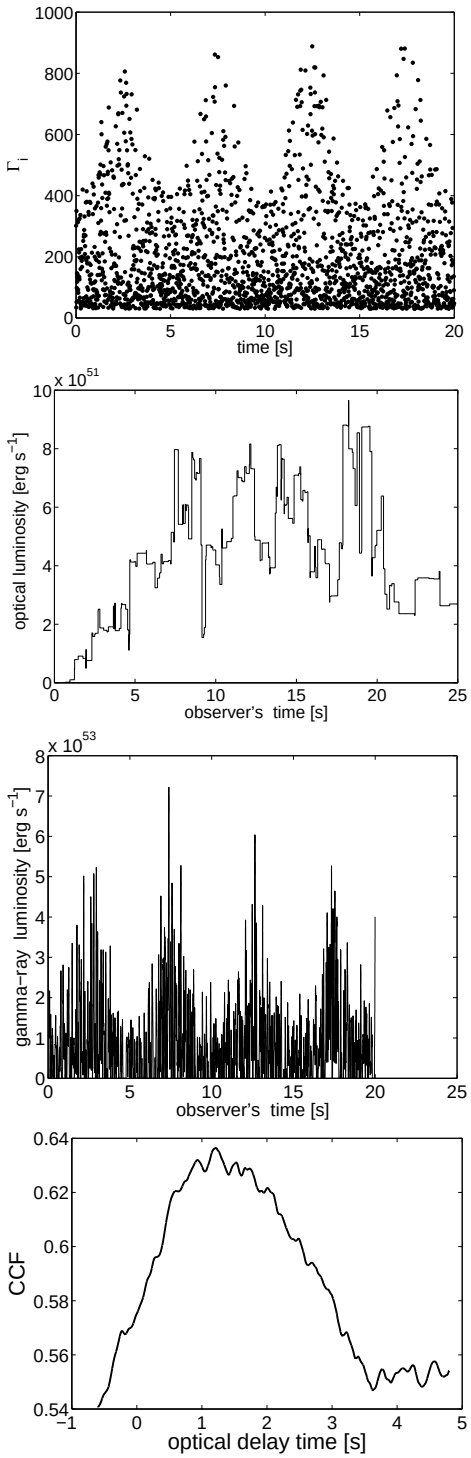

Fig. 6 Results of Test 5, as a comparison with GRB 080319B (fig. 2 in Beskin et al. 2010). The respective panels represent the same quantities as in Fig. 1.

5 DISCUSSION

The simple model we proposed is able to explain the basic temporal structure of diverse GRB prompt emission. By adjusting the initial variations in velocity, i.e., the initial LF distribution in the outflow, our simulations can reproduce the complex variability features in realistic light curves. One can predict the highly variable temporal profile by controlling the initial variance of the shell velocities, and more importantly, inspecting the observed temporal features in the light curves of separate energy bands allows us to assess the central engine activity in detail.

The central engine activity and its detailed properties regulate the temporal variations displayed in the sequence of shells injected from the central engine, which are then reflected in the observed variability components in the light curves. For GRB 080319B, we require at least two timescales of the central engine activity to reproduce the observed optical light curve, which is an important implication of its central engine. In the current situation, we are not able to identify what causes these two timescales. However, following the common picture of the collapsar model, a new black hole, with a surrounding torus, is formed in the center of the progenitor star. For a black hole of $\sim 3m_3 M_\odot$, the accretion time of material at the innermost radius $r_{\rm in}$ of the torus is $t_{\rm acc} \sim 2m_3$ ms (e.g., Narayan et al. 2001), comparable to the small timescale we require, whereas the accretion time at the outer radius $r_{\rm out} \sim 10^2 r_{\rm in}$ is $t_{\rm acc} \sim 4m_3(r_{\rm out}/10^2 r_{\rm in})^{3/2}$s (Narayan et al. 2001), similar to the larger timescale. This may imply that the supply of material at the outer edge of the torus is non-stable.

An important feature shown in our simulated results is the time delay between the optical and gamma-ray light curves due to the larger radius of the optical emission region. The delay time is about 1 s in all the tests. The optical delay has been predicted by Li & Waxman (2008) in the single timescale case. They show that for optical emission to avoid the synchrotron self absorption, the outflow needs to expand to larger radii of $R \sim 10^{15} R_{15}$ cm, and hence the optical delay time is $\Delta t \sim R/2\langle\Gamma\rangle^2\, c \sim 1 R_{15}(\langle\Gamma\rangle/10^2)^{-2}$ s, where $\langle\Gamma\rangle$ is the average value for initial LFs of the ejected shells. This is comparable to the resulting delay time in the tests. However, since many factors can influence the delay time, more systematic simulations are required to investigate the dependence of the delay time on the input parameters in future work.

6 CONCLUSIONS

Starting with a two-component LF distribution of the shells injected from the central engine, our simulations generated the optical and gamma-ray light curves both from a superposition of two variability components with different timescales. The slow component has the same timescale as that exhibited in the initial LFs, but the time scale of the fast component has a trend with energy: the gamma-ray light curve has much more and faster short-scale variabilities than its optical counterpart. Moreover, the timescale of the fast variability shows changes with time in the simulated optical light curve. The value in the first 20 s of the light curve is one order of magnitude smaller than that of the other part, which is in agreement with the finding in Margutti et al. (2008).

The similarity between the optical and gamma-ray light curves, and the time delay between them, provides strong evidence that the emission has a common origin, but is generated at different radii from the central engine. Further discussions show that the light curves of prompt emission actually provide the temporal information to clarify the physical nature of the central engine. The different variability components seen in the light curves depend on the intrinsic variability with different timescales of the internal engine. Detailed temporal analysis of the simulated light curves is necessary and will be performed in our future work.

Hopefully, more observations with high temporal resolution of prompt optical emission from GRBs will be acquired by future telescopes, e.g., UFFO-Pathfinder (Chen 2011) and SVOM-GWAC (Paul et al. 2011). These well-sampled bursts will further test the validity of our model and provide deeper insight into behavior of the source.

Acknowledgements This work has been supported in part by the National Natural Science Foundation of China (Grant No. 11273005), Specialized Research Fund for the Doctoral Program of Higher Education (SRFDP), China (20120001110064), the CAS Open Research Program of Key Laboratory for the Structure and Evolution of Celestial Objects, and the National Basic Research Program of China (973 Program, 2014CB845800).

Appendix A:

We derive the width of the merged shell after shock crossings. Consider two colliding shells, with the lab-frame width Δ_i and LF γ_i, where $i = 1, 2$. Shell 2 is faster, and overtakes shell 1. There are double shocks and four regions in the interaction. The unshocked shells 1 and 2 have number densities n_1 and n_2, respectively, in their own rest frame. The densities in the forward and reverse shock regions are $n_f = 4\gamma_f n_1$ and $n_r = 4\gamma_r n_2$, respectively, in their own rest frame, where $\gamma_{f,r}$ are the LFs of the shocked fluid relative to unshocked shells 1 and 2, respectively,

$$\gamma_f = \gamma_1\gamma_{\rm cm}(1-\beta_1\beta_{\rm cm}),\ \ \gamma_r = \gamma_2\gamma_{\rm cm}(1-\beta_2\beta_{\rm cm})\,. \tag{A.1}$$

Note there is no relative motion between the forward and reverse shock regions.

Now consider everything in one frame, which is better to be the lab frame. In the lab frame, the unshocked shell 1, shocked fluid (both forward and reverse shock regions) and unshocked shell 2 have LFs γ_1, $\gamma_{\rm cm}$ and γ_2 respectively. So in the lab frame, the densities of the four regions are, going inward, $\gamma_1 n_1$, $\gamma_{\rm cm} n_f$, $\gamma_{\rm cm} n_r$ and $\gamma_2 n_2$. The compression factor, i.e. the factor that the density is enhanced by the shock, is $k_f = \gamma_{\rm cm} n_f/(\gamma_1 n_1) = 4\gamma_f\gamma_{\rm cm}/\gamma_1$ for the forward shock region, or $k_r = \gamma_{\rm cm} n_r/(\gamma_1 n_1) = 4\gamma_r\gamma_{\rm cm}/\gamma_2$ for the reverse shock region. Thus the shock-compressed, merged shell has a width, right after merging without spreading, of

$$\Delta_c = \frac{\Delta_1}{k_f} + \frac{\Delta_2}{k_r} = \frac{\Delta_1\gamma_1}{4\gamma_f\gamma_{\rm cm}} + \frac{\Delta_2\gamma_2}{4\gamma_r\gamma_{\rm cm}} = \frac{1}{4\gamma_{\rm cm}^2}\left(\frac{\Delta_1}{1-\beta_1\beta_{\rm cm}} + \frac{\Delta_2}{1-\beta_2\beta_{\rm cm}}\right)\,. \tag{A.2}$$

References

Abdo, A. A., Ackermann, M., Ajello, M., et al. 2009a, ApJ, 706, L138
Abdo, A. A., Ackermann, M., Ajello, M., et al. 2009b, Nature, 462, 331
Akerlof, C., Balsano, R., Barthelmy, S., et al. 1999, Nature, 398, 400
Beloborodov, A. M. 2010, MNRAS, 407, 1033
Beskin, G., Karpov, S., Bondar, S., et al. 2010, ApJ, 719, L10
Chen, P. 2011, International Cosmic Ray Conference, 8, 240, arXiv:1106.3929
Cui, X.-H., Li, Z., & Xin, L.-P. 2013, RAA (Research in Astronomy and Astrophysics), 13, 57
Derishev, E. V., Kocharovsky, V. V., & Kocharovsky, V. V. 2001, A&A, 372, 1071
Fan, Y.-Z., Zhang, B., & Wei, D.-M. 2009, Phys. Rev. D, 79, 021301
Guetta, D., Spada, M., & Waxman, E. 2001, ApJ, 557, 399
Huang, Y.-F., Lu, Y., Wong, A. Y. L., & Cheng, K. S. 2007, ChJAA (Chin. J. Astron. Astrophys.), 7, 397
Kobayashi, S., Piran, T., & Sari, R. 1997, ApJ, 490, 92
Kopač, D., Kobayashi, S., Gomboc, A., et al. 2013, ApJ, 772, 73
Li, Z. 2010, ApJ, 709, 525
Li, Z., & Waxman, E. 2008, ApJ, 674, L65
Lyutikov, M., & Blandford, R. 2003, arXiv:astro-ph/0312347
Margutti, R., Guidorzi, C., Chincarini, G., et al. 2008, in American Institute of Physics Conference Series, 1065, eds. Y.-F. Huang, Z.-G. Dai, & B. Zhang, 259

Mészáros, P., & Rees, M. J. 2000, ApJ, 530, 292
Narayan, R., & Kumar, P. 2009, MNRAS, 394, L117
Narayan, R., Piran, T., & Kumar, P. 2001, ApJ, 557, 949
Page, K. L., Willingale, R., Osborne, J. P., et al. 2007, ApJ, 663, 1125
Paul, J., Wei, J., Basa, S., & Zhang, S.-N. 2011, Comptes Rendus Physique, 12, 298
Pe'er, A., & Zhang, B. 2006, ApJ, 653, 454
Piran, T., Sari, R., & Zou, Y.-C. 2009, MNRAS, 393, 1107
Racusin, J. L., Karpov, S. V., Sokolowski, M., et al. 2008, Nature, 455, 183
Rees, M. J., & Meszaros, P. 1994, ApJ, 430, L93
Shen, R.-F., Song, L.-M., & Li, Z. 2005, MNRAS, 362, 59
Shen, R.-F., & Zhang, B. 2009, MNRAS, 398, 1936
Thompson, C. 1994, MNRAS, 270, 480
Usov, V. V. 1994, MNRAS, 267, 1035
Vestrand, W. T., Wozniak, P. R., Wren, J. A., et al. 2005, Nature, 435, 178
Wang, X.-Y., Li, Z., Dai, Z.-G., & Mészáros, P. 2009, ApJ, 698, L98
Waxman, E. 2003, in Supernovae and Gamma-Ray Bursters, Lecture Notes in Physics, 598, ed. K. Weiler, 393 (Berlin: Springer Verlag)
Yost, S. A., Swan, H. F., Rykoff, E. S., et al. 2007, ApJ, 657, 925
Zhang, B., & Yan, H. 2011, ApJ, 726, 90
Zhao, X. H., Li, Z., Liu, X. W., et al. 2013, arXiv:1310.0551
Zou, Y.-C., Piran, T., & Sari, R. 2009, ApJ, 692, L92